Flat-Field Correction Pipeline for a Cone-Beam Computed Tomography Imaging Device with Independently Movable Source and Detector

Peter Keuschnigg[1], Philipp Steininger[1,2], Horst Schoedl[2], Katja Presich[1], Daniel Kellner[1,2], Philipp Huber[1], Ulrich Mayer[1,2], Markus Mehrwald[1,2], and Heinz Deutschmann[1,2]

[1] Paracelsus Medical University, Institute for Research and Development on Advanced Radiation Technologies (radART), Strubergasse 16, 5020 Salzburg, Austria
[2] medPhoton GmbH, Strubergasse 16, 5020 Salzburg, Austria

Abstract. The ImagingRing, a novel cone-beam computed tomography (CBCT) imaging device with independently rotatable x-ray source and flat-panel detector arms, allows for planar and CBCT acquisitions of arbitrary regions inside the device's cylindrical imaging volume. Due to its special geometry, an adjustment of standard methods for generating flat-field planar images is required in order to fit the particular geometric conditions. This work gives an overview of the current implementation of the flat-field correction pipeline for the ImagingRing as well as an outlook to further planned improvements for CBCT enhancing quality.

1 Introduction

The ImagingRing [1,2], a cone-beam computed tomography (CBCT) imaging device, has recently been developed by medPhoton GmbH which is a spin-off company of the Paracelsus Medical University. This novel device is a couch-mounted scanner with independently rotatable x-ray source and flat-panel detector arms, which allow for special use cases in conventional and particle radiotherapy. The scanner is moveable along the couch to allow for covering all relevant anatomical regions and the x-ray beam is shaped with a source-mounted 2D collimator. Supporting independent rotations, the ImagingRing is capable of performing planar and CBCT x-ray acquisitions focusing on arbitrary regions inside the cylindrical imaging volume. Due to the ImagingRing's special geometry, an adjustment of standard methods for generating flat-field planar images is required in order to fit the particular geometric conditions.

This work gives an overview of the current implementation of the flat-field correction pipeline integrated in the open-radART ion software suite [4] for the ImagingRing as well as an outlook to further planned improvements.

2 Methods

The pipeline for flat-field correction of planar images acquired with the ImagingRing consists of several customized standard methods. In a first step the multi-level-

gain (MLG) correction is responsible for creating dose-equivalent images by accounting for the non-linear dose response of the flat-panel detector. A subsequent bad-pixel correction handles outlier intensities resulting from dysfunctional pixels or sectors of the detector. Afterwards, the images are oriented in the device's imaging coordinate system (ICS) using a flexmap calibration to account for the gravity-induced flex of the source and detector arms. After successful image orientation, the projections are corrected for the beam fluence of the x-ray source. Finally, beam attenuation caused by varying incidence angles and source-to-detector distance (SDD) is accounted for.

2.1 Geometry of the ImagingRing

The basic geometry of the ImagingRing is defined as shown in Figure 1. S denotes the position of the x-ray source focal spot and R denotes the flat panel detector image origin. The unit vectors v_1 and v_2 depict the detector row and column orientation vectors, respectively. The mechanical isocenter (ISO) is different from the virtual axis of rotation N. The SDD measured from S to the detector center C usually cannot be considered constant, due to the possibility of independent rotations for imaging a region around an arbitrary point N. Even in an opposite position, where the isocenter is on the line between S and C, v_1 is not perpendicular to this line to enable for large-field-of-view CBCT acquisitions. Hence, for simplification of post-processing (e.g. reconstruction) the images are projected on a consensus plane which is perpendicular to $\overline{SISO}$.

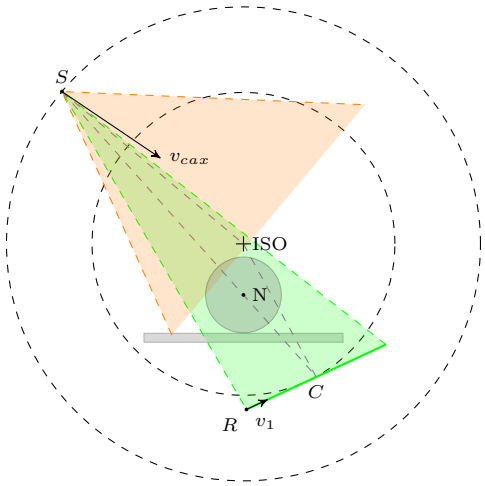

Fig. 1: ImagingRing geometry for an acquisition of a region around the effective imaging isocenter N, showing the focal spot position S, the detector origin R, the detector center C and orientation vector v_1 with respect to the table and a cylindrical phantom object.

2.2 Multi-Level-Gain Correction

As described in Huber et al. [3], MLG correction is used for correcting the nonlinear detector response, especially at low dose rates. For this method, an offset image without irradiation and multiple flood-field gain images at different dose rates are acquired. In contrast to the application for other imaging devices, the flood-field MLG calibration for the ImagingRing is more complex since a short SDD results in varying incidence angles of the x-rays at the detector. To overcome this limitation a slit collimation is utilized, allowing for irradiation of just a few columns of the detector while rotating the detector through the slit. Each column is irradiated with the same slit beam profile, avoiding the requirement of correcting for the inhomogeneous fluence of the x-ray tube in rotation direction. Since the source-mounted 2D collimator allows for arbitrary jaw positions, it can be used to form a slit with adjustable size. The mean value of the intensities for which a specific pixel on the detector has been irradiated then defines its intensity on the MLG calibration image as shown in Figure 2a. The beam profile at calibration time normalized in the range $[0.0, 1.0]$, which is visualized in Figure 2b, can be extracted from the MLG calibration image.

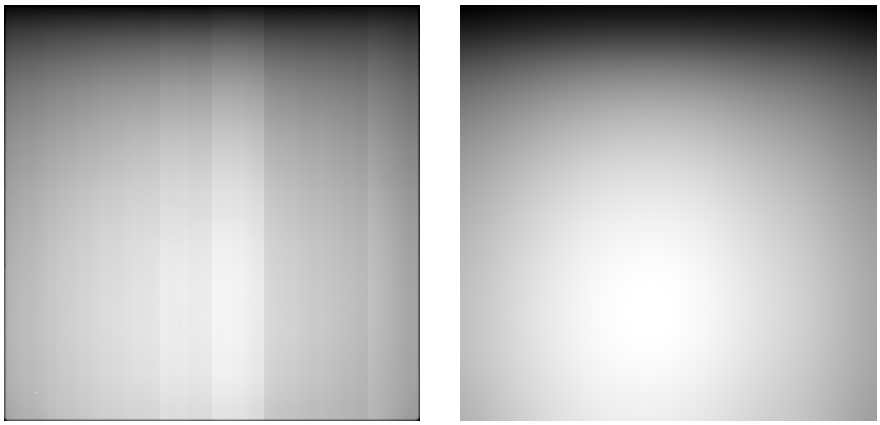

(a) MLG calibration image (b) calibration beam profile

Fig. 2: MLG calibration image (a) which has been generated from slit collimation acquisitions of the ImagingRing, showing different intensity levels for sub-panels. The beam-profile (b) extracted from the MLG image is used for correcting the beam-dependent intensity variations due to, e.g., the anode heel effect.

The correction method itself has been implemented similar to what is described in Huber et al. [3]. Using the MLG supporting points measured at multiple known dose-rates, a nonlinear mapping between a pixel intensity and a specific dose rate value can be performed, resulting in a dose-equivalent inten-

sity. For a given intensity at the detector I_d, the dose-equivalent intensity D_d is computed by linear interpolation between the closest MLG calibration images (high, low) followed by a correction for the calibration beam profile D_{calib}.

$$D_d = \frac{D_{low} + (I_d - I_{low})\frac{D_{high} - D_{low}}{I_{high} - I_{low}}}{D_{calib}} \quad : I_{low} \leq I_d \leq I_{high} \tag{1}$$

2.3 BadPixel Correction

A pixel on the detector p_d is considered bad if its intensity deviation from the surrounding pixel intensities U is greater than a given intensity threshold I_t. Static bad pixels are present in all acquisitions, whereas dynamic bad pixels appear and vanish at certain energy levels. Therefore, the calibration of this method consists of acquisition of homogeneous frames at multiple beam energies and subsequent evaluation of the outliers in each image. Hence, the resulting binary bad-pixel map in which non-zero pixels identify bad pixels is computed by:

$$I_b = \begin{cases} 0, & \text{if } |I_i - I_d| \leq I_t \quad \forall I_i \in U \\ 1, & \text{otherwise} \end{cases} \tag{2}$$

The correction method utilizes a spiral interpolation approach of n intensities of the original image for replacing the intensities of marked bad pixels defined in (2). The intensity sampling is started at a random angle and continues with golden angle increments and progressive distance p_d. For each interpolated intensity I_i, the Euclidean distance to p_d is used as a weighting factor w_i. The replacement intensity is then computed by the weighted mean value of the interpolated intensities given in (3).

$$I_c = \sum_{i=1}^{n} w_i I_i \quad \text{where } \sum_{i=1}^{n} w_i = 1 \tag{3}$$

2.4 Image Orientation and Flexmap Correction

For further corrections, the acquired image has to be oriented in the ICS. In order to account for dynamic movement of the source- and panel-arms due to gravity based effects, a 9-degrees-of-freedom (9-DOF) flexmap is applied. The 9-DOF flexmap specifies for combinations of source and panel arm positions a vector $[tS_x, tS_y, tS_z]$ for translations of S, a vector $[tC_x, tC_y, tC_z]$ for translations of C and a set of 3 Euler angles for transformation of v_1 and v_2. This approach is similar to what has been described in Warmerdam et al. [5] for investigating geometric uncertainties in 2D/3D image registration of cranial images.

2.5 Incidence Angle Correction

For a single ray emerging from the focal spot position S and passing through a specific detector pixel, the acquired intensity at the detector is attenuated

depending on the incidence angle α and the beam energy E. The correction of the former effect is referred to as geometric incidence angle correction whereas the latter is referred to as physical incidence angle correction. Measurements for different energies $E = \{60kV, 120kV\}$ and various angles $\alpha \in [-40\,\text{deg}, 40\,\text{deg}]$ to account for the maximum field-of-view have shown the separability of those effects.

The geometric incidence angle correction as shown in (6) can be seen as a relative correction from a pixel position at a given detector plane p_d to another plane p_c (e.g. the consensus plane) using the incidence angles α_d and α_c respectively. Specifically, α depends on S, its projection onto the specific plane S_d, S_c and the point on the plane p_d, p_c.

$$\alpha_d = \arctan\left(\frac{||S - S_d||}{||p_d - S_d||}\right) \tag{4}$$

$$\alpha_c = \arctan\left(\frac{||S - S_c||}{||p_c - S_c||}\right) \tag{5}$$

$$I_c = I_d \frac{\cos(\alpha_c)}{\cos(\alpha_d)} \tag{6}$$

The physical incidence angle correction can be seen as the deviation of the measured angle dependency from the cosine function, depending on the used energy E and the incidence angle α. Having specified the measurements in a polynomial of degree four for a low energy $Y_{low}(x) = 1 + c_{2low}x^2 + c_{4low}x^4$ and a high energy $Y_{high}(x) = 1 + c_{2high}x^2 + c_{4high}x^4$, a linear interpolation for arbitrary energies is used for the correction:

$$I_c = \frac{I_d}{Y_{low}(\alpha) + (Y_{high}(\alpha) - Y_{low}(\alpha))\frac{E - E_{low}}{E_{high} - E_{low}}} \tag{7}$$

2.6 Distance Correction

The intensity produced on the detector surface is dependent on the distance of the focal spot to the specific detector pixel. Projecting the intensities from a pixel position at the detector plane p_d onto another plane p_c (e.g. consensus plane) therefore requires a relational correction according to the inverse square law. Using the Euclidean distance $d(p, q) = ||p - q||$ from the focal spot S, the equation can be stated as:

$$I_c = I_d \frac{||p_d - S||^2}{||p_c - S||^2} \tag{8}$$

2.7 Fluence Correction

For the calibration of the fluence correction, multiple projections are taken such that the whole cone has been imaged at least once. A continuous detector movement as described for MLG calibration can be used again for this acquisition.

The acquired images are subsequently pre-processed by bad-pixel correction and MLG correction. The fluence plane is defined perpendicular to v_{cax} at the isocenter. A stitched projection of all pre-processed images onto the fluence plane considering flex calibration, incidence angle correction and distance correction followed by a normalization to the range $[0.0, 1.0]$ creates the fluence map. A fluence map as shown in Figure 3 is created for multiple energies E. For a given position of a pixel at the detector p_d, the most relevant fluence map, i.e. closest matching E, for the given energy is evaluated at a point p_f which is the intersection of a ray between S and p_d with the fluence plane. The evaluated intensity is subsequently corrected for the geometric incidence angle and the distance of the detector plane before using it for the correction, as stated in (9).

$$I_c = \frac{I_d}{I_f \frac{\cos(\alpha_d)}{\cos(\alpha_f)} \frac{||p_f - S||^2}{||p_d - S||^2}} \tag{9}$$

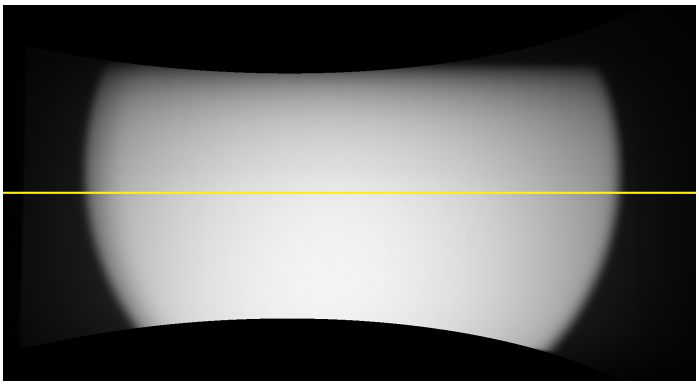

Fig. 3: Fluence map for 120kV with a source cone angle of 50 deg which is used for fluence correction. The anode heel effect is visible at the top of the cone. The yellow line represents the horizontal intensity profile extracted in Figure 4.

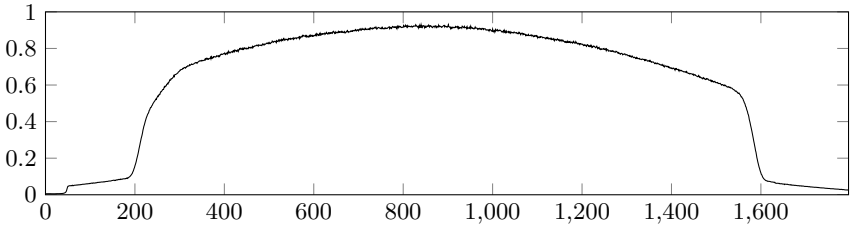

Fig. 4: Horizontal intensity profile of the fluence map for 120kV with a source cone angle of 50 deg.

3 Results

An acquisition of images with the ImagingRing at various positions of the source and detector arm show clearly an effect of the specific geometry to the intensity profile, as can be seen in Figure 5a, Figure 6 and Figure 7. After correcting the images with the proposed pipeline, the bad-pixels and differences in sub-panel intensity levels have been removed as shown in Figure 5b, Figure 6 and Figure 7. Furthermore, the impact of the geometric effects and the heel effect as part of the beam fluence have been minimized. Especially in the homogeneous table region, the flattening of the intensity profiles is obvious. However, even though the vertical intensity profile of the corrected table image shows a straightened curve, there is a remaining slope visible. In the left lower corner of the images, the cone border is visible since the 9DOF-flexmap correction does not account for a flex induced tilt of v_{cax}, effectively leading to an insufficient fluence correction.

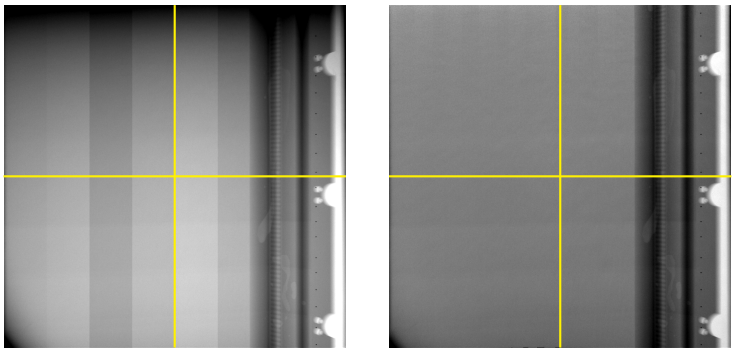

(a) original (b) corrected

Fig. 5: A planar x-ray acquisition of the couch carrying the ImagingRing before (a) and after (b) the application of the correction pipeline. The yellow lines represent the horizontal (Figure 6) and vertical (Figure 7) intensity profile positions.

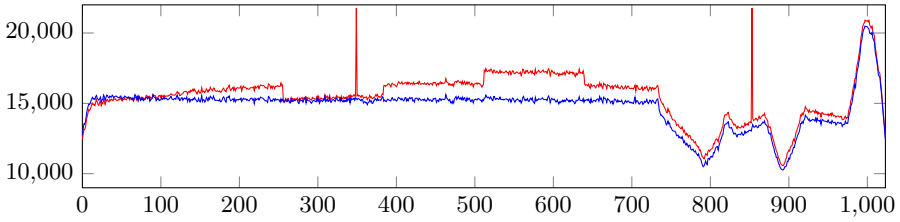

Fig. 6: Comparison of the horizontal beam profiles from the images of Figure 5 before (red) and after (blue) application of the correction pipeline.

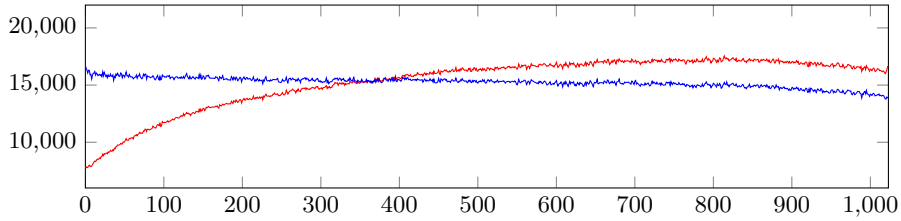

Fig. 7: Comparison of the vertical beam profiles from the images of Figure 5 before (red) and after (blue) application of the correction pipeline.

4 Discussion

As successfully shown in the results section, the presented correction pipeline is able to handle x-ray acquisitions created by arbitrary source and panel arm positions. However, the offset response of the flat-panel detector used for MLG-correction may change over time due to reasons of varying detector temperature and age factors. Since the detector response is non-linear especially in a range close to the offset value, a dynamic replacement of the offset values is considered critical for long-term operation of the device and currently under investigation. For the case of CBCT acquisitions, a basic lag correction may also be added to the correction pipeline. However, the dynamic offset replacement can be seen as a prerequisite for successful ghosting correction. The use case of CBCT reconstruction with correct hounsfield units in addition requires for a scatter correction considering head scatter and patient scatter as key factors. A replacement of the 9DOF-flexmap correction with an 11DOF equivalent, additionally accounting for tilts of v_{cax}, is currently examined. Future developments may also include advanced temperature correction algorithms as have been described in Huber et. al [3] for electronic portal imaging.

5 Acknowledgments

This work was supported by grant $I1383 - B23$ (DEXTER project) of the Austrian Science Fund (FWF).

References

1. Deutschmann, H.: Patient positioning and imaging system. European Patent EP 2687159 A1 (2013)
2. Deutschmann, H., Neuner, M., Steininger, P., Pinzger, M., Buck, M., Sedlmayer, F.: Robotic positioning and imaging. Strahlenther Onkol. 2013 189(2), 185–185 (2013)
3. Huber, S., Mooslechner, M., Mitterlechner, B., Weichenberger, H., Serpa, M., Sedlmayer, F., Deutschmann, H.: Image quality improvements of electronic portal imaging devices by multi-level gain calibration and temperature correction. Physics in Medicine and Biology 58(18), 6429–6446 (2013)

4. Steininger, P., Mehrwald, M., Neuner, M., Kellner, D., Memelink, M., Pinzger, M., Böhler, A., Mitterlechner, B., Keuschnigg, P., Weichenberger, H., Sedlmayer, F., Deutschmann, H., et al.: The open-radart ion (oraion) software suite. In: National Institue of Radiological Sciences & EBG MedAustron GmbH (Hrsg.) editors(s). Joint Symposium on Carbon Ion Radiotherapy. pp. 157–167. Wr. Neustadt (2014)
5. Warmerdam, G., Steininger, P., Neuner, M., Sharp, G., Winey, B.: Influence of imaging source and panel position uncertainties on the accuracy of 2D3d image registration of cranial images. Med. Phys. 39(9), 5547–5556 (2012)